INTERNATIONAL JOURNAL FOR NUMERICAL METHODS IN FLUIDS
Int. J. Numer. Meth. Fluids 2010; **63**:96–118
Published online 20 May 2009 in Wiley InterScience (www.interscience.wiley.com). DOI: 10.1002/fld.2080

An efficient scaled boundary FEM model for wave interaction with a nonuniform porous cylinder

Hao Song[1] and Longbin Tao[2,*,†]

[1]*Griffith School of Engineering, Gold Coast Campus, Griffith University, QLD 4222, Australia*
[2]*School of Marine Science and Technology, Newcastle University, Newcastle NE1 7RU, U.K.*

SUMMARY

The scaled boundary finite-element method (SBFEM) by Tao *et al.* (*Comput. Methods Appl. Mech. Engrg* 2007; **197**:232–242) is only applicable for wave scattering problems by a structure of homogenous material. In this paper, the SBFEM is extended to deal with the interaction of water waves and porous offshore structure with a partially solid wall or opening. The cylindrical structure is considered as a circular cylinder of anisotropic material in the form of variable porosity. A central feature of the newly extended method is that the non-homogenous term caused by the complex configuration of the structure is processed by introducing a variable porous-effect parameter G. This leads to the final scaled boundary finite-element equation is still homogenous and can be solved in a similar manner. The modified SBFEM thus remains a semi-analytical fundamental-solution-less method. Numerical experiments in water wave interaction with a typical coastal/offshore structure—a cylinder with a partially solid wall or opening attest to the efficacy and accuracy of the proposed approach. Copyright © 2009 John Wiley & Sons, Ltd.

Received 12 September 2008; Revised 4 March 2009; Accepted 4 April 2009

KEY WORDS: scaled boundary finite-element method; short-crested wave; wave diffraction; unbounded domain; nonuniform porous cylinder; wave–structure interaction

1. INTRODUCTION

In order to reduce the direct wave impact and resonance from occurring, coastal and offshore structures are often constructed with protective porous layers. Owing to its scientific and engineering significance, wave motion through a porous structure has attracted considerable attention. For many years, there have been a widespread applications of porous structures in coastal and offshore engineering. For example, porous breakwaters are commonly constructed to protect coasts and harbours; The concentric porous cylinder system—Ekofisk gravity offshore structure was built with an porous exterior layer to protect interior column in the North Sea (see Figure 1). However,

*Correspondence to: Longbin Tao, School of Marine Science and Technology, Newcastle University, Newcastle NE1 7RU, U.K.
†E-mail: L.Tao@ncl.ac.uk

Figure 1. Ekofisk gravity structure (Courtesy ConocoPhillps).

the understanding of the phenomenon is still far from complete. Among many issues, the ability of a coastal and ocean engineer to predict wave transmission and diffraction, hence the wave elevation, wave forces and the stability of the structures, plays a central role in the protection of the structures [1].

Chwang [2] proposed a linearized porous-wavemaker theory to analyse small amplitude surface waves produced by horizontal oscillations of a porous vertical plate. The theory was later applied to analyse surface waves generated by a piston-type porous wavemaker near the end of a semi-infinitely long channel of constant depth [3]. Several studies on the physical phenomenon of wave trapping due to a porous plate or a concentric porous cylinder system using the porous-wavemaker theory were reported (e.g. [4, 5]).

Dalrymple *et al.* [6] studied the reflection and transmission of a wave train at an oblique angle of incidence by an infinitely long porous breakwater. Yu and Chwang [7] performed extensive study on the transmission characteristics of waves past a porous structure. The wave behaviour within the porous medium was also investigated. It was found that there is an optimum thickness for a porous structure beyond which any further increase of the thickness may not lead to an appreciable improvement in reducing its transmission and reflection characteristics. Yu and Chwang [8] employed the boundary integral method to study wave diffraction by a horizontal porous plate submerged at a distance below the free surface in a fluid of constant depth. Wang and Ren [9] also studied the performance of a flexible and porous breakwater. Additional related work can be found in the review article of Chwang and Chan [1].

One of the noticeable limitations in the previous studies is the two-dimensional plane wave assumption. Wind-generated waves in real oceans are much better represented by short-crested waves (3D) than by plane waves (2D) [10, 11]. Short-crested waves commonly arise from the oblique interaction of two travelling plane waves or intersecting swell waves, from the reflection of waves at non-normal incidence off a vertical seawall or a breakwater, as well as from diffraction about the surface boundaries of a structure of finite length. Such a 3D waves are of paramount importance in coastal and offshore structure design.

Recently, a semi-analytical method, called scaled boundary finite-element method (SBFEM) for solving linear partial differential equations has found successful applications to soil–structure

DOI: 10.1002/fld

interaction problems. The SBFEM method was proposed by Song and Wolf [12] and systematically described by Wolf [13]. Combining the distinct advantages of the finite-element (FEM) and boundary-element methods (BEM), only the structure boundary is discretized with surface finite elements. This, in turn, transforms the governing partial differential equations to a set of ordinary differential equations, and solves them analytically. The method represents singularities and unbounded domains accurately and efficiently when compared with the complete FEM and requires no fundamental solution as needed by the BEM. Fewer elements are required to obtain very accurate results [13].

Only recently the SBFEM has been applied to wave diffraction in which the radiation condition at infinity is required to be satisfied by the scattered waves. Li *et al.* [14] solved the problem of plane wave diffraction by a vertical cylinder using SBFEM. Similar to the approach of Wolf [13] in obtaining a solution for soil–structure interaction, Li *et al*. [14] adopted an algebraic series to obtain the final solution. However, for low-frequency waves, the series hardly converges to the exact solution.

Tao *et al.* [15] developed a modified SBFEM model and applied it to solve short-crested wave interaction with a circular cylinder. Instead of using a power series as proposed in the original SBFEM, Tao *et al.* [15] chose Hankel function as a base function to solve the 2D Helmholtz equation in the unbounded domain. As a direct consequence of such a modification, the radial differential equation is solved fully analytically in all frequency ranges. Without relying on any other numerical schemes, the semi-analytical model for the short-crested wave diffraction by a single circular cylinder is shown to reproduce the analytical solution for all physical properties including wave run-up, effective inertia and drag coefficients, and total force very accurately at very low computational cost.

However, the methodology proposed by Tao *et al.* [15] is only suitable for a closed circular cylinder. If a cylinder is not closed, e.g. has openings, the final scaled boundary finite-element equation (SBFEE) becomes non-homogeneous, rising much difficulty in the solution procedure. The goal of this paper is to solve this physical problem in the same efficient way as presented in [15]. By introducing a porous-effect parameter G (Chwang's parameter), the structure is treated as a nonuniform porous cylinder. We will show that the final SBFEE derived is still homogeneous and can be solved in a similar way as proposed in our previous work [15]. The modified SBFEM thus remains a semi-analytical fundamental-solution-less method. The newly developed approach is then applied to solve short-crested wave interaction with a cylindrical structure of variable porosity in the circumferential direction. Convergence tests are given to demonstrate the accuracy and efficiency of the numerical model. Only a few finite elements discretized on the circumference of the cylinder are shown to be sufficient to obtain accurate results. Detailed numerical results on wave forces and surface elevations over a broad range of incident wave parameters and structure configuration including the cylinder radius, structural porosity, opening angle and location on the wave elevation and forces are examined in detail.

2. THEORETICAL FORMULATION OF THE BOUNDARY VALUE PROBLEM (BVP)

We consider a monochromatic short-crested wave train propagating in the direction of the positive x axis. A vertical porous cylindrical structure extends from the sea bottom to above the free surface of the ocean along the z axis. The origin is placed at the centre of the cylinder on the mean water surface (Figure 2). The fluid domain is divided into two regions, an interior region Ω_1 and a region

DOI: 10.1002/fld

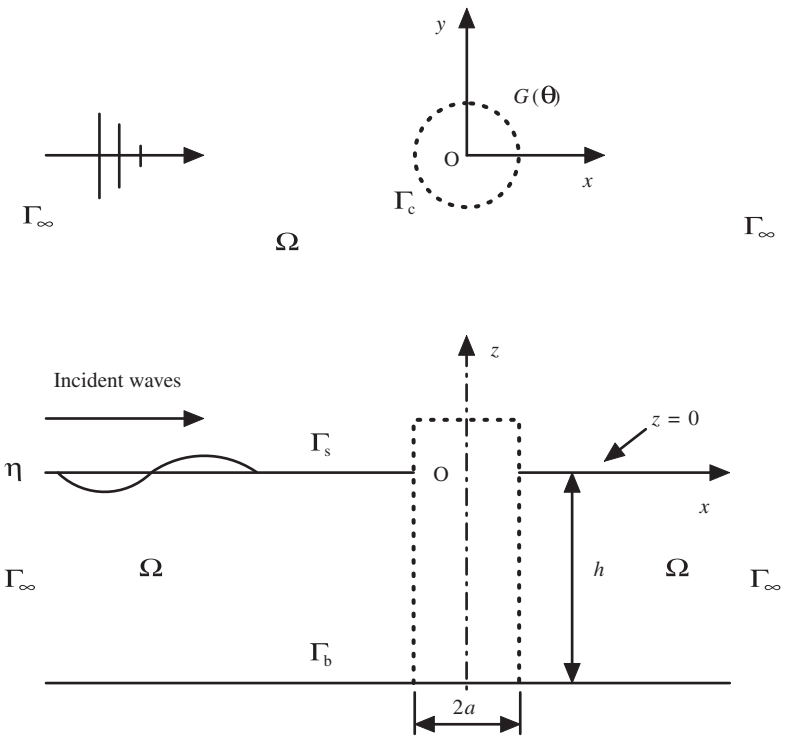

Figure 2. Definition sketch of wave interaction with a porous cylindrical structure.

outside the cylinder Ω_2. The following notations have been used in the paper: $\Phi_j =$ total velocity potential, $\Phi^I =$ velocity potential of incident wave, $\Phi^S =$ velocity potential of scattered wave, $k =$ total wave number, $k_x =$ wave number in x direction, $k_y =$ wave number in y direction, $\omega =$ wave frequency, $h =$ water depth, $A =$ amplitude of incident wave, $a =$ cylinder radius, $t =$ time, $\rho =$ mass density of water and $g =$ gravitational acceleration. The subscripts $j\,(j=1,2)$ denote the physical parameters in the region $\Omega_j\,(j=1,2)$.

Assuming the fluid to be inviscid, incompressible and the flow to be irrotational, the fluid motion can be described by a velocity potential Φ_j satisfying the Laplace equation

$$\nabla^2\Phi_j = 0 \quad \text{in } \Omega_j \tag{1}$$

subject to the combined-free surface boundary condition

$$\Phi_{j,tt} + g\Phi_{j,z} = 0 \quad \text{at } z=0 \tag{2}$$

and the bottom condition

$$\Phi_{j,z} = 0 \quad \text{at } z=-h \tag{3}$$

where the comma in the subscript designates partial derivative with respect to the variable following the comma.

DOI: 10.1002/fld

The velocity potentials can be decomposed by separating the vertical variable z and the time t from each component as

$$\Phi_j(x,y,z,t)=\phi_j(x,y)Z(z)\mathrm{e}^{-\mathrm{i}\omega t} \quad \text{in } \Omega_j \tag{4}$$

$$\Phi_2^I(x,y,z,t)=\phi_2^I(x,y)Z(z)\mathrm{e}^{-\mathrm{i}\omega t} \quad \text{in } \Omega_2 \tag{5}$$

$$\Phi_2^S(x,y,z,t)=\phi_2^S(x,y)Z(z)\mathrm{e}^{-\mathrm{i}\omega t} \quad \text{in } \Omega_2 \tag{6}$$

where

$$Z(z)=\frac{\cosh k(z+h)}{\cosh kh} \tag{7}$$

This procedure leads to the sea bottom condition being automatically satisfied, while the linearized free surface boundary condition is satisfied using the following dispersion relationship:

$$\omega^2=gk\tanh kh \tag{8}$$

The total velocity potential in the outer region Ω_2 is given as a linear sum of the scattered wave potential and the incident wave potential

$$\Phi_2=\Phi_2^I+\Phi_2^S, \quad \phi_2=\phi_2^I+\phi_2^S \quad \text{in } \Omega_2 \tag{9}$$

Taylor [16] showed that the fluid flow passing through the porous boundary can be essentially assumed to obey Darcy's law if the boundary is made of fine pores. Hence, the porous flow velocity is linearly proportional to the pressure difference between the two sides of the porous boundary, and the boundary condition on porous cylinder can be expressed as [2]

$$\phi_{1,n}=-\phi_{2,n}=\mathrm{i}G(\theta)k(\phi_1-\phi_2) \quad \text{on } r=a \tag{10}$$

where $G(\theta)$ is a measure of the porous effect, named as Chwang's parameter. For a cylinder of nonuniform porosity, $G(\theta)$ varies along the circumferential direction. For special cases, $G=0,\infty$ represent a cylinder with a partial solid wall and a partial opening, respectively [2].

The BVP becomes two dimensional at the free surface. The function $\phi_2^S(x,y)$ in the unbounded domain Ω_2 is governed by the Helmholtz equation with the boundary condition at the interface of fluid and porous cylinder, and the radiation condition at infinity, namely the Sommerfeld condition as follows:

$$\nabla^2\phi_2^S+k^2\phi_2^S=0 \quad \text{in } \Omega_2 \tag{11}$$

$$\phi_{2,n}^S=-\mathrm{i}G(\theta)k(\phi_1-\phi_2^S-\phi_2^I)-\phi_{2,n}^I \quad \text{on } r=a \tag{12}$$

$$\lim_{kr\to\infty}(kr)^{1/2}(\phi_{2,r}^S-\mathrm{i}k\phi_2^S)=0 \quad \text{in } \Omega_2 \tag{13}$$

where r is the radial axis, and $\mathrm{i}=\sqrt{-1}$.

The function $\phi_1(x,y)$ in the bounded domain Ω_1 is governed by the Helmholtz equation with the boundary condition at the interface of fluid and porous cylinder at $r=a$:

$$\nabla^2\phi_1+k^2\phi_1=0 \quad \text{in } \Omega_1 \tag{14}$$

DOI: 10.1002/fld

$$\phi_{1,n} = \mathrm{i}G(\theta)k(\phi_1 - \phi_2^S - \phi_2^I) \quad \text{on } r = a \tag{15}$$

The velocity potential of the linear short-crested incident wave travelling principally in the positive x direction is given by the real part of [17]

$$\Phi_I = -\frac{\mathrm{i}gA}{\omega} Z(z) \mathrm{e}^{\mathrm{i}(k_x x - \omega t)} \cos(k_y y) \quad \text{in } \Omega_2 \tag{16}$$

Equations (11)–(15) constitute two sets of the governing equation and boundary conditions for the diffraction of short-crested waves by a vertical porous cylindrical structure, corresponding to BVPs in a bounded domain and an unbounded domain, respectively. After obtaining ϕ_2^S, Φ_2 and Φ_1 by solving the above BVPs, the velocity, free surface elevation and the dynamic pressure can be calculated, respectively, from

$$\mathbf{v}_j = \nabla \Phi_j \tag{17}$$

$$\eta_j = \frac{\mathrm{i}\omega}{g} \phi_j \tag{18}$$

$$p_j = -\rho \Phi_{j,t} \tag{19}$$

3. SCALED BOUNDARY TRANSFORMATION

In this section, ϕ_1 and ϕ_2^S will both be denoted as ϕ for brevity, and the region Ω_j will be denoted as Ω. If the velocity boundary is defined by Γ_v, we have

$$\phi_{,n} = \bar{v}_n \quad \text{on } \Gamma_v \tag{20}$$

where the overbar denotes a prescribed value.

The FEM requires the weighted residuals of the governing equation to be zero. Hence, Equations (11), (14) and (20) are multiplied by a weighting function w and integrated over the flow domain and the boundary. Performing integration by parts, the resulting equation becomes

$$\int_\Omega \nabla^{\mathrm{T}} w \nabla \phi \, \mathrm{d}\Omega - \int_\Omega w k^2 \phi \, \mathrm{d}\Omega - \oint_\Gamma w \bar{v}_n \, \mathrm{d}\Gamma = 0 \tag{21}$$

SBFEM defines the domain Ω by scaling a single piecewise-smooth curve S relative to a scaling centre (x_0, y_0), which is chosen at the cylinder centre in this case (see Figure 3). The circumferential coordinate s is anticlockwise along the curve S and the normalized radial coordinate ξ is a scaling factor, defined as 1 at curve S and 0 at the scaling centre. The whole solution domain Ω is in the range of $\xi_0 \leqslant \xi \leqslant \xi_1$ and $s_0 \leqslant s \leqslant s_1$. The two straight sections $s = s_0$ and $s = s_1$ are called side-faces. They coincide if the curve S is closed. For bounded domain, $\xi_0 = 0$ and $\xi_1 = 1$, whereas for unbounded domain, $\xi_0 = 1$ and $\xi_1 = \infty$. Therefore, the Cartesian coordinates are transformed to the scaled boundary coordinate ξ and s with the scaling equations

$$x = x_0 + \xi x_s(s), \quad y = y_0 + \xi y_s(s) \tag{22}$$

By employing SBFEM, an approximate solution of ϕ is sought as

$$\phi_A(\xi, s) = \mathbf{N}(s)\mathbf{a}(\xi) \tag{23}$$

DOI: 10.1002/fld

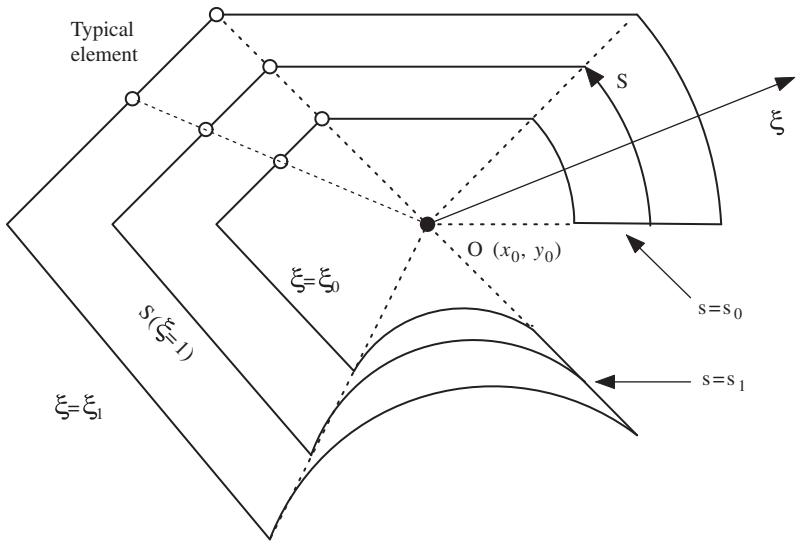

Figure 3. The coordinate definition of SBFEM.

where $\mathbf{N}(s)$ is the shape function, the vector $\mathbf{a}(\xi)$ is analogous to the nodal values same as in FEM. The radial function $a_j(\xi)$ represents the variation of the wave potential in the radial axis ξ at each node j, and the shape function $\mathbf{N}(s)$ interpolates between the nodal potential values in the circumferential axis s.

Performing the scaled boundary transformation [15], we have

$$\mathbf{E}_0\xi^2\mathbf{a}(\xi)_{,\xi\xi}+(\mathbf{E}_0+\mathbf{E}_1^{\mathrm{T}}-\mathbf{E}_1)\xi\mathbf{a}(\xi)_{,\xi}-\mathbf{E}_2\mathbf{a}(\xi)+k^2\xi^2\mathbf{M}_0\mathbf{a}(\xi)=\xi\mathbf{F}_s(\xi) \tag{24}$$

subject to the boundary conditions

$$\mathbf{E}_0\xi_0\mathbf{a}(\xi_0)_{,\xi}+\mathbf{E}_1^{\mathrm{T}}\mathbf{a}(\xi_0)=-\int_S\mathbf{N}(s)^{\mathrm{T}}(\bar{v}_n(\xi_0,s))\xi_0\,\mathrm{d}s \tag{25}$$

$$\mathbf{E}_0\xi_1\mathbf{a}(\xi_1)_{,\xi}+\mathbf{E}_1^{\mathrm{T}}\mathbf{a}(\xi_1)=\int_S\mathbf{N}(s)^{\mathrm{T}}(\bar{v}_n(\xi_1,s))\xi_1\,\mathrm{d}s \tag{26}$$

where

$$\mathbf{E}_0=\int_S\mathbf{B}_1(s)^{\mathrm{T}}\mathbf{B}_1(s)|J|\mathrm{d}s \tag{27}$$

$$\mathbf{E}_1=\int_S\mathbf{B}_2(s)^{\mathrm{T}}\mathbf{B}_1(s)|J|\mathrm{d}s \tag{28}$$

$$\mathbf{E}_2=\int_S\mathbf{B}_2(s)^{\mathrm{T}}\mathbf{B}_2(s)|J|\mathrm{d}s \tag{29}$$

$$\mathbf{M}_0=\int_S\mathbf{N}(s)^{\mathrm{T}}\mathbf{N}(s)|J|\mathrm{d}s \tag{30}$$

DOI: 10.1002/fld

$$\mathbf{F}_s(\xi)=\mathbf{N}(s_0)^{\mathrm{T}}(-\bar{v}_n(\xi,s_0))|J(s_0)|+\mathbf{N}(s_1)^{\mathrm{T}}(-\bar{v}_n(\xi,s_1))|J(s_1)| \tag{31}$$

$$\mathbf{B}_1(s)=\mathbf{b}_1(s)\mathbf{N}(s), \quad \mathbf{B}_2(s)=\mathbf{b}_2(s)\mathbf{N}(s)_{,s} \tag{32}$$

$$\mathbf{b}_1(s)=\frac{1}{|J|}\begin{Bmatrix} y_s(s)_{,s} \\ -x_s(s)_{,s} \end{Bmatrix}, \quad \mathbf{b}_2(s)=\frac{1}{|J|}\begin{Bmatrix} -y_s(s) \\ x_s(s) \end{Bmatrix} \tag{33}$$

and $|J|$ is the Jacobian at the boundary

$$|J|=x_s(s)y_s(s)_{,s}-y_s(s)x_s(s)_{,s} \tag{34}$$

Equation (24) is the so-called SBFEE, which is non-homogeneous because of the term $\mathbf{F}_s(\xi)$ arising from the structure configuration, e.g. cylinder with an opening. In the present approach, by introducing the variable porous parameter, the cylindrical structure can then be treated as a closed cylinder of variable porosity. Thus, the side-faces in the scaled boundary finite element coordinate system coincide. Since the flow across the side-faces is equal and opposite, the term $\mathbf{F}_s(\xi)$ vanishes. Therefore, the final governing equation, Equation (24), is a homogeneous second-order ordinary matrix differential equation in terms of matrix.

Boundary conditions, Equations (12) and (13) or (15), are weakened in the form of Equations (25) and (26), respectively, indicating the relationship between the integrated nodal flow on the boundary and the velocity potentials of the nodes. For the wave diffraction problem in the unbounded region Ω_2, $\xi_0=1$ on the boundary of porous cylinder and $\xi_1=+\infty$ at infinity. For the BVP in the bounded region Ω_1, $\xi_0=0$ and $\xi_1=1$.

4. SOLUTION PROCEDURE

For a circular cylinder, we have

$$x_s(s)=a\cos(s/a), \quad y_s(s)=a\sin(s/a) \tag{35}$$

From Equations (22), (33), (34), (32) and (27)–(28), $x_s(s)_{,s}$, $y_s(s)_{,s}$, $\mathbf{b}_1(s)$, $\mathbf{b}_2(s)$, $|J|$, $\mathbf{B}_1(s)$, $\mathbf{B}_2(s)$, $\mathbf{E}_0$, $\mathbf{E}_1$, $\mathbf{E}_2$ and $\mathbf{M}_0$ can be calculated accordingly. The following relationships hold:

$$\mathbf{E}_1=0\cdot\mathbf{I}, \quad \mathbf{E}_0^{-1}\mathbf{M}_0=a^2\mathbf{I} \tag{36}$$

$$\mathbf{E}_0=\frac{1}{a}\int_S \mathbf{N}(s)^{\mathrm{T}}\mathbf{N}(s)\,\mathrm{d}s \tag{37}$$

where $\mathbf{I}$ is the identity matrix of rank m.

Using Equation (36), pre-multiplying both sides of Equation (24) by $\mathbf{E}_0^{-1}$ and simplifying, we have

$$\zeta^2\mathbf{a}(\zeta)_{,\zeta\zeta}+\zeta\mathbf{a}(\zeta)_{,\zeta}-\mathbf{E}_0^{-1}\mathbf{E}_2\mathbf{a}(\zeta)+\zeta^2\mathbf{a}(\zeta)=0 \tag{38}$$

where

$$\zeta=ka\xi \tag{39}$$

DOI: 10.1002/fld

4.1. Solution for unbounded domain Ω_2

Equation (38) is the matrix form of Bessel's differential equation. Considering the Sommerfeld radiation condition equation (13), here we select $H_{r_j}(\zeta)\mathbf{T}_j$ as a base solution of Equation (38) in the unbounded region Ω_2.

The solution for $\mathbf{a}_2(\zeta)$ is then expressed in the series form

$$\mathbf{a}_2(\zeta)=\sum_{j=1}^{m} c_j H_{r_j}(\zeta)\mathbf{T}_j=\mathbf{T}\mathbf{H}(\zeta)\mathbf{C} \tag{40}$$

in which $\mathbf{T}_j$ are vectors of rank m, c_j are coefficients, $H_{r_j}(\zeta)$ are the Hankel functions of the first kind, and

$$\mathbf{T}=[\mathbf{T}_1,\mathbf{T}_2,\ldots,\mathbf{T}_m] \tag{41}$$

$$\mathbf{H}(\xi)=\mathrm{diag}[H_{r_1}(ka\xi),H_{r_2}(ka\xi),\ldots,H_{r_m}(ka\xi)] \tag{42}$$

$$\mathbf{C}=[c_1,c_2,\ldots,c_m]^{\mathrm{T}} \tag{43}$$

where 'diag' denotes a diagonal matrix with the elements in the square brackets on the main diagonal.

Substituting Equation (40) into (38), and using the following properties of Hankel function:

$$\zeta^2 H''_{r_j}(\zeta)=-\zeta^2 H_{r_j}(\zeta)+\zeta H_{r_j+1}(\zeta)-r_j H_{r_j}(\zeta)+r_j^2 H_{r_j}(\zeta) \tag{44}$$

$$\zeta H'_{r_j}(\zeta)=-\zeta H_{r_j+1}(\zeta)+r_j H_{r_j}(\zeta) \tag{45}$$

where the prime and the double prime denote the first and second derivatives with respect to the argument ζ, respectively, we have

$$\sum_{j=1}^{m}(\mathbf{E}_0^{-1}\mathbf{E}_2-r_j^2\mathbf{I})\mathbf{T}_j\cdot c_j H_{r_j}(\zeta)=0 \tag{46}$$

For any $c_j H_{r_j}(\zeta)$, Equation (46) yields

$$(\mathbf{E}_0^{-1}\mathbf{E}_2-r_j^2\mathbf{I})\mathbf{T}_j=0 \tag{47}$$

Let λ_j be the eigenvalues of $\mathbf{E}_0^{-1}\mathbf{E}_2$, then $r_j=\sqrt{\lambda_j}$, and $\mathbf{T}_j$ are the eigenvectors of $\mathbf{E}_0^{-1}\mathbf{E}_2$.

Since the Sommerfeld radiation condition (13) has been satisfied by the Hankel functions, we now only consider the body boundary condition (25) of the circular cylinder

$$\mathbf{E}_0 ka\sum_{j=1}^{m} c_j H'_{r_j}(ka)\mathbf{T}_j=-\left[\int_S \mathbf{N}(s)^{\mathrm{T}}\mathbf{N}(s)\,\mathrm{d}s\right]\bar{\mathbf{v}}_{2n}^{S} \tag{48}$$

where $\bar{\mathbf{v}}_{2n}^{S}$ is the vector of nodal normal velocity of scattered wave in region Ω_2 on the body boundary.

DOI: 10.1002/fld

4.2. Solution for bounded domain Ω_1

Similar approach is applied to the region Ω_1. Assume

$$\mathbf{a}_1(\zeta)=\sum_{j=1}^{m} c_j^1 J_{r_j}(\zeta)\mathbf{T}_j=\mathbf{T}\mathbf{J}(\zeta)\mathbf{C}^1 \tag{49}$$

where c_j^1 are coefficients, $J_{r_j}(\zeta)$ are the Bessel functions of the first kind, and

$$\mathbf{C}^1=[c_1^1, c_2^1, \ldots, c_m^1]^{\mathrm{T}} \tag{50}$$

$$\mathbf{J}(\xi)=\mathrm{diag}[J_{r_1}(ka\xi), J_{r_2}(ka\xi), \ldots, J_{r_m}(ka\xi)] \tag{51}$$

Again if λ_j are the eigenvalues of $\mathbf{E}_0^{-1}\mathbf{E}_2$, then $r_j=\sqrt{\lambda_j}$, and $\mathbf{T}$ is the eigenvector of $\mathbf{E}_0^{-1}\mathbf{E}_2$.

Applying boundary condition on the porous cylinder equation (26), we have

$$\mathbf{E}_0 ka\mathbf{T}\mathbf{J}_a'\mathbf{C}^1=\left[\int_S \mathbf{N}(s)^{\mathrm{T}}\mathbf{N}(s)\,\mathrm{d}s\right]\bar{\mathbf{v}}_{1n} \tag{52}$$

where $\bar{\mathbf{v}}_{1n}$ is the vector of nodal total normal velocity in region Ω_1 on the body boundary of porous cylinder.

Combining Equations (10), (20), (23), (37), (40), (48), (49) and (52), and noting

$$\bar{\mathbf{v}}_{2n}^I+\bar{\mathbf{v}}_{2n}^S=\bar{\mathbf{v}}_{2n}=-\bar{\mathbf{v}}_{1n} \tag{53}$$

where $\bar{\mathbf{v}}_{2n}^I$ is the vector of nodal normal velocity of incident wave in the region Ω_2 on the body boundary of the porous cylinder, $\mathbf{a}_1(\xi)$ and $\mathbf{a}_2(\xi)$ are solved as

$$\mathbf{a}_1(\xi)=\mathbf{T}\mathbf{J}(\xi)\mathbf{W}^{-1}(\mathbf{T}^{-1}\bar{\mathbf{a}}_2^I+\mathbf{H}_{ah}\mathbf{T}^{-1}\bar{\mathbf{v}}_{2n}^I/k) \tag{54}$$

$$\mathbf{a}_2(\xi)=\mathbf{T}\mathbf{H}_h(\xi)(\mathbf{J}_a'\mathbf{W}^{-1}\mathbf{T}^{-1}\bar{\mathbf{a}}_2^I+\mathbf{H}_{ah}^{-1}\mathbf{V}\mathbf{W}^{-1}\mathbf{H}_{ah}\mathbf{T}^{-1}\bar{\mathbf{v}}_{2n}^I/k) \tag{55}$$

where

$$\mathbf{V}=\mathrm{i}\mathbf{T}^{-1}\mathbf{G}^{-1}\mathbf{T}\mathbf{J}_a'+\mathbf{J}_a \tag{56}$$

$$\mathbf{W}=\mathbf{V}-\mathbf{H}_{ah}\mathbf{J}_a' \tag{57}$$

and

$$\mathbf{J}_a=\mathrm{diag}[J_{r_1}(ka), J_{r_2}(ka), \ldots, J_{r_m}(ka)] \tag{58}$$

$$\mathbf{J}_a'=\mathrm{diag}[J_{r_1}'(ka), J_{r_2}'(ka), \ldots, J_{r_m}'(ka)] \tag{59}$$

$$\mathbf{H}_h(\xi)=\mathrm{diag}[H_{r_1}(ka\xi)/H_{r_1}'(ka), H_{r_2}(ka\xi)/H_{r_2}'(ka), \ldots, H_{r_m}(ka\xi)/H_{r_m}'(ka)] \tag{60}$$

$$\mathbf{H}_{ah}=\mathrm{diag}[H_{r_1}(ka)/H_{r_1}'(ka), H_{r_2}(ka)/H_{r_2}'(ka), \ldots, H_{r_m}(ka)/H_{r_m}'(ka)] \tag{61}$$

$\mathbf{G}$ is a diagonal matrix where the value on the diagonal designates the porosity G in the corresponding elements.

Using Equations (4), (5), (16), (20) and (23), $\bar{\mathbf{v}}_{2n}^I$ and $\bar{\mathbf{a}}_2^I$ can be easily determined on the porous cylinder boundary. From Equations (6), (9), (23), (54) and (55), the approximation of velocity potential in both region Ω_1 and region Ω_2 can be obtained.

DOI: 10.1002/fld

All the other physical properties of engineering interest including velocity, surface elevation and pressure can now be determined based on the velocity potentials by Equations (17)–(19). The total force per unit length on the cylinder in the $u(u=x, y)$ direction is then calculated as

$$\frac{\mathrm{d}F_u}{\mathrm{d}z} = -a\int_0^{2\pi} p\cdot\cos(\theta)\,\mathrm{d}\theta = 2\pi a P_u(k_x, k_y, k, a)\cdot\rho g A\cdot Z(z)\mathrm{e}^{-\mathrm{i}\omega t} \tag{62}$$

where the function $P_u(k_x, k_y, k, a)$ is the dimensionless parameter of $\mathrm{d}F_u/\mathrm{d}z$ without the term $\rho g A\cdot Z(z)\mathrm{e}^{-\mathrm{i}\omega t}$.

The function $P_u(k_x, k_y, k, a)$ determines the first-order total horizontal force in the u direction on the cylinder, F_u, which can be obtained by integrating Equations (62) with respect to z

$$F_u = \int_{-h}^{0}\frac{\mathrm{d}F_u}{\mathrm{d}z}\,\mathrm{d}z = 2\pi a P_u(k_x, k_y, k, a)\cdot\rho g A\mathrm{e}^{-\mathrm{i}\omega t}\cdot\tanh(kh)/k \tag{63}$$

The total moment about an axis parallel to the y-axis passing through the bottom of the cylinder is

$$M_y = \int_{-h}^{0}(z+h)\frac{\mathrm{d}F_x}{\mathrm{d}z}\,\mathrm{d}z = 2\pi a P_x(k_x, k_y, k, a)\cdot\rho g A\mathrm{e}^{-\mathrm{i}\omega t}\cdot f(kh)/k^2 \tag{64}$$

$$M_x = -\int_{-h}^{0}(z+h)\frac{\mathrm{d}F_y}{\mathrm{d}z}\,\mathrm{d}z = 2\pi a P_y(k_x, k_y, k, a)\cdot\rho g A\mathrm{e}^{-\mathrm{i}\omega t}\cdot f(kh)/k^2 \tag{65}$$

where

$$f(kh) = [kh\tanh(kh) + \mathrm{sech}(kh) - 1] \tag{66}$$

It can be concluded from Equations (63)–(65) that only the functions $P_x(k_x, k_y, k, a)$ and $P_y(k_x, k_y, k, a)$ need to be discussed.

5. VALIDATION OF SBFEM MODEL

As a first step to ensure the convergence of the solution to be found, it is essential to examine the detailed relationship between the number of elements required on the cylinder surface and ka. The SBFEM model described in the previous section is then further validated with theoretical solutions [18]. For the physical problem with symmetric properties, only half the cylinder needs to be discretized. In this paper, the cylinder circumference is discretized with three-node quadratic elements (see Figure 4).

Figure 5 shows the convergence of the surface elevation at the origin and wave forces in relation to ka for a cylinder with uniform porosity ($G_0=1$). It is clearly seen in Figure 5(a) that even 2 elements lead to very accurate results of elevations for ka up to 1.8, while 4 and 6 elements are required to produce valid solutions in the range of $ka\leqslant 5.2$ and $ka\leqslant 8.4$, respectively. As can be seen in Figure 5(b), the convergence zone of ka for wave force calculation is notably broader.

Figure 6 shows surface elevation at the origin (left) and wave forces (right) versus non-dimensional radius ka for a cylinder with nonuniform porosity ($G_0=1$ and $G_1=10$) along the circumferential direction. Three types of the configuration are considered, i.e. the region of the partial porosity G_1 lies in (a) $[\pi/2, 3\pi/2]$; (b) $[3\pi/4, 5\pi/4]$; (c) $[7\pi/8, 9\pi/8]$, respectively.

DOI: 10.1002/fld

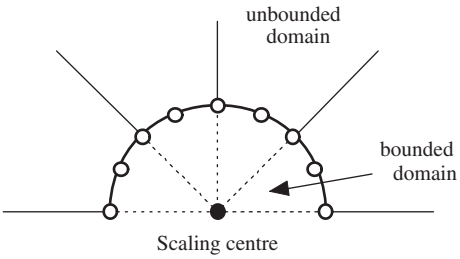

Figure 4. Scaled boundary finite element mesh for a porous cylindrical structure.

Again, only half of the cylinder surface needs to be discretized. As shown in Figures 6(a) and (d), even 4 elements are seen to produce very accurate results of surface elevation and wave force for ka up to 4. A general trend that more elements are required for increasing ka are clearly seen in the figures. For both surface elevation and wave force calculations, Figure 6 shows that the difference between the present SBFEM solutions with 8 elements and analytical solutions is indistinguishable for ka up to 10 for all three configurations presented.

For the physical problems of non-symmetric configurations, whole cylinder needs to be discretized along the circumferential direction, thus the number of required elements doubles. Figure 7 shows the convergence of elevation and wave forces for a cylinder with a partial opening in $[3\pi/4, \pi]$ interaction with the incoming short-crested waves of equal wave numbers in two perpendicular directions. The two different porosities are $G_1 = +\infty$ in $[3\pi/4, \pi]$ and $G_0 = 1$ in the rest of the cylinder. It can be seen in Figure 7 that 16 elements (corresponding to 8 elements in the half cylinder) are adequate to achieve relatively high accuracy for calculation of both elevation and wave forces in the range of $ka \leqslant 10$. For elevation, 8 elements (corresponding to 4 elements in the half cylinder) exhibit excellent agreement with the analytical solutions until $ka = 5.3$. Since the physical problem is no longer symmetric to the x axis, wave force in the y direction comes forth with rather smaller magnitude compared with the inline force.

6. NUMERICAL RESULTS AND DISCUSSION

6.1. Surface elevation

6.1.1. Influence of ka. The equi-amplitude (left) and equi-phase (right) contours for incident short-crested wave having the wave number $k_x = k_y = \sqrt{2}/2\,\mathrm{m}^{-1}$, interaction with a porous cylinder ($G_0 = 1$) with a partial opening at $7/8\pi < \theta < 9/8\pi$, for $a = 2, 3, 4\,\mathrm{m}$ are shown in Figure 8. The thick lines in phase contours represent changes from π to $-\pi$. It can be seen clearly that the wave patterns inside the porous cylinder become more complex as a increases, with increases in density of both the amplitude and phase contours. This is mainly due to more physical space for the waves transmitted into the interior region to develop. Amphidromic points come forth when the bounded area is adequately large to form them.

6.1.2. Influence of G_0. The equi-amplitude (left) and equi-phase (right) contours for incident short-crested wave ($k_x = k_y = \sqrt{2}/2\,\mathrm{m}^{-1}$) interaction with a cylinder ($a = 4\,\mathrm{m}$) of three different porosities $G_0 = 0.5, 1, 10$, with a partial opening at $7/8\pi < \theta < 9/8\pi$, are shown in Figure 9. As can

DOI: 10.1002/fld

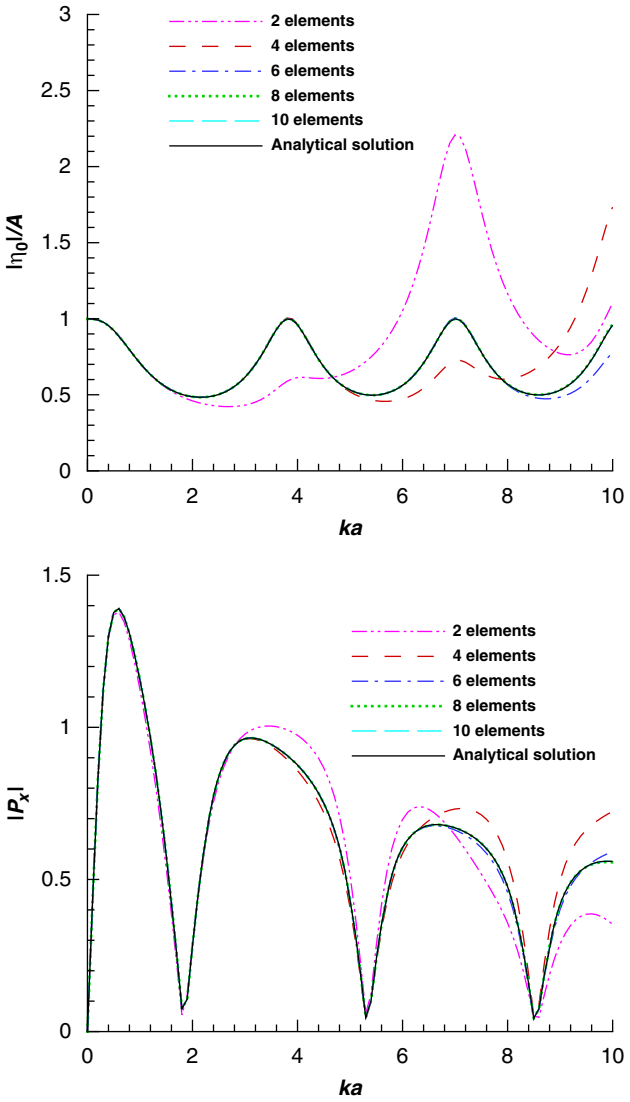

Figure 5. Surface elevation at the origin and wave forces versus ka for short-crested wave ($k_x = k_y$) interaction with a porous cylinder of uniform porosity $G_0 = 1$.

be seen from the figure, the wave pattern is more complex as the porosity G_0 is smaller due to the stronger interaction of the waves reflected by the internal surface of the cylinder. As porosity G_0 increases, the effect of diffraction weakens and the cylinder becomes transparent gradually, leading to a wave pattern similar to that of a progressive wave.

6.1.3. Influence of opening angle. Figure 10 shows the equi-amplitude (left) and equi-phase (right) contours for short-crested wave ($k_x = k_y = \sqrt{2}/2\,\mathrm{m}^{-1}$) interaction with a porous cylinder ($a = 4\,\mathrm{m}$ and $G_0 = 1$) with a partial opening centred at $\beta = \pi$ for three different opening angles $\alpha = \pi/4, \pi/2, \pi$.

DOI: 10.1002/fld

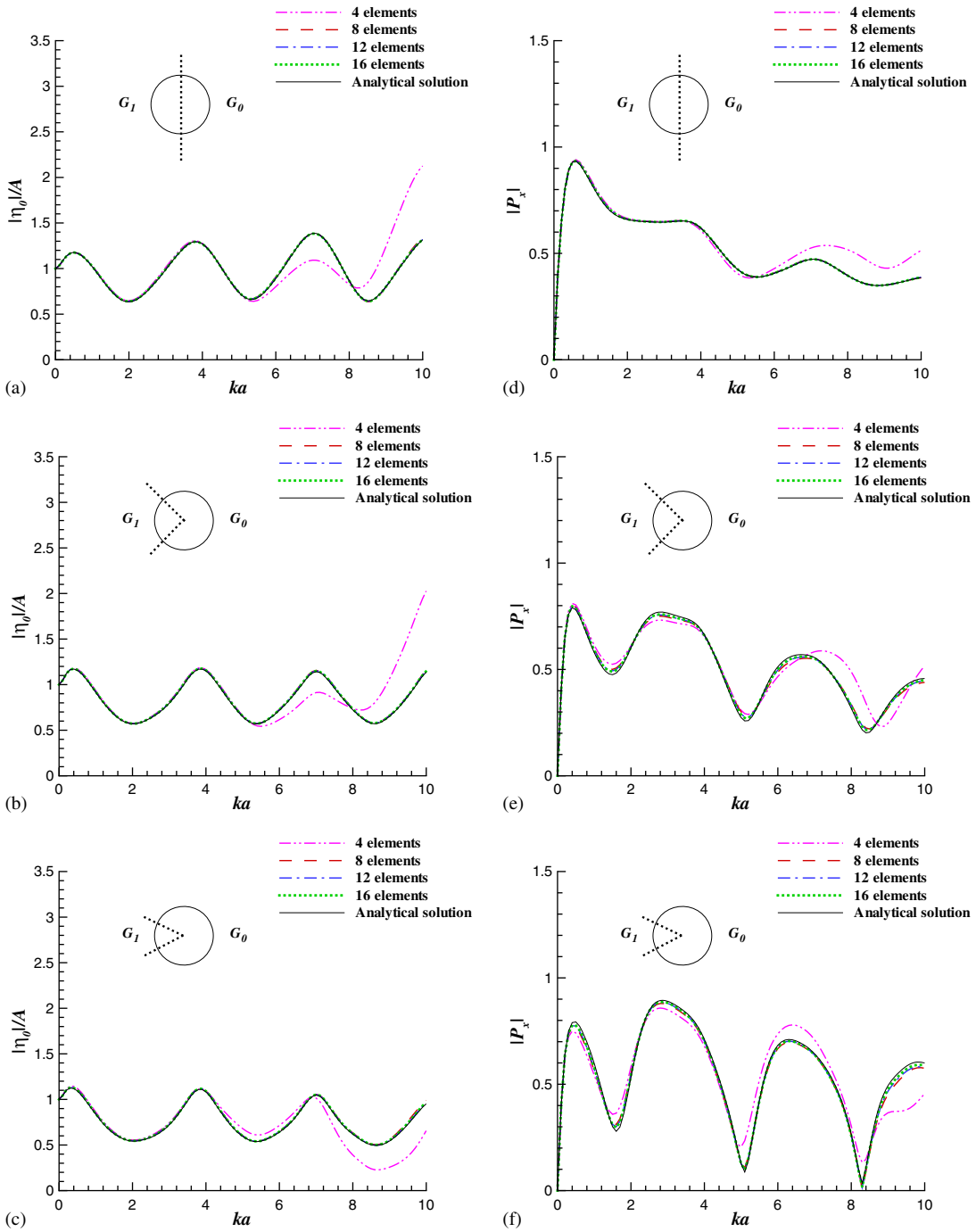

Figure 6. Surface elevation at the origin (left) and wave forces (right) versus ka for short-crested wave ($k_x = k_y$) interaction with a porous cylinder of nonuniform porosity $G_0 = 1$ and $G_1 = 10$.

DOI: 10.1002/fld

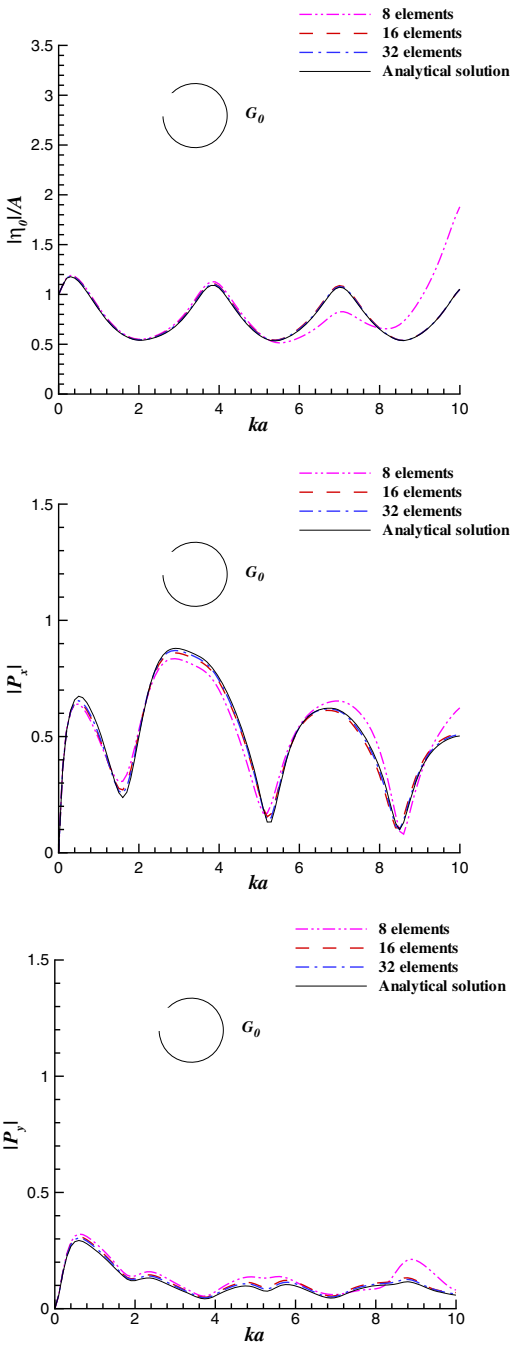

Figure 7. Surface elevation at the origin and wave forces versus ka for short-crested wave ($k_x = k_y$) interaction with a porous cylinder ($G_0 = 1$) with a partial opening at $[3\pi/4, \pi]$.

DOI: 10.1002/fld

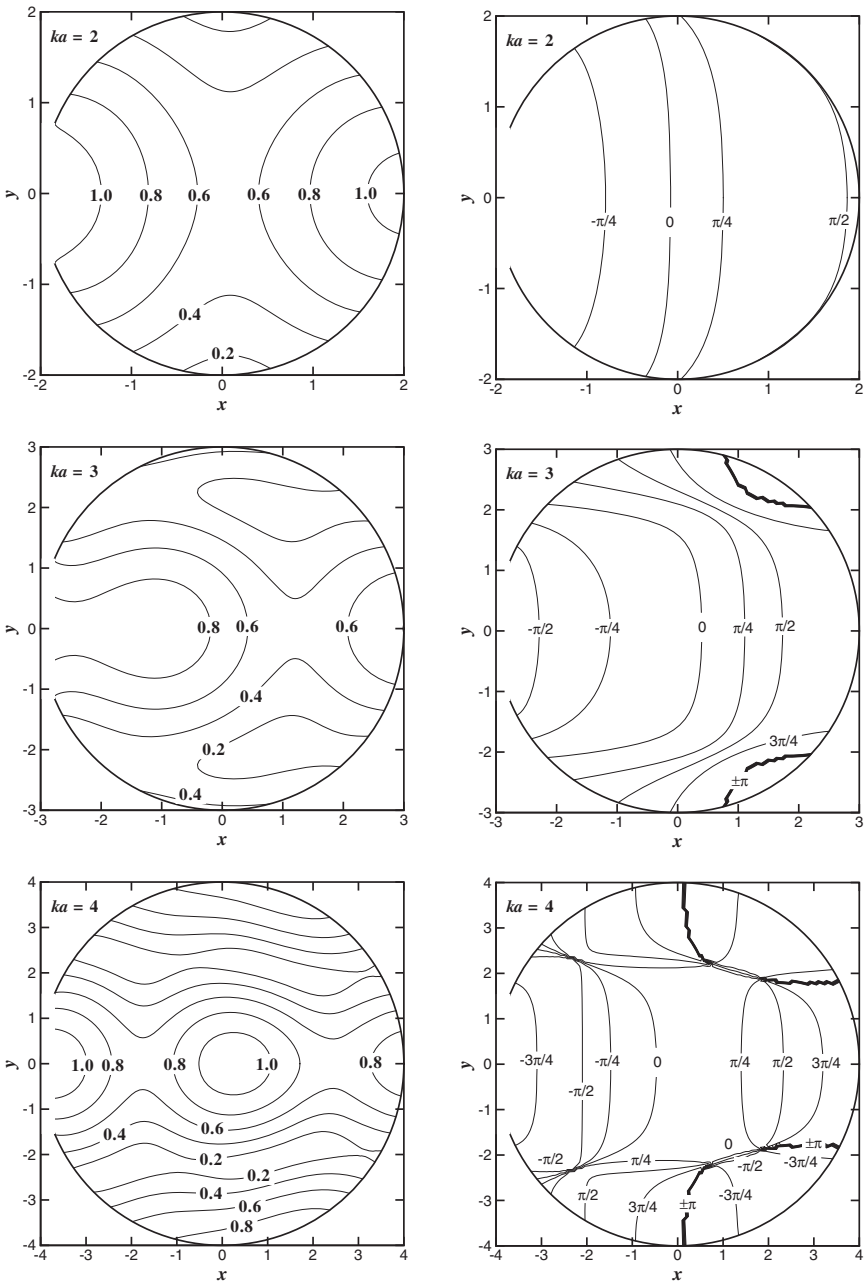

Figure 8. Equi-amplitude (left) and equi-phase (right) contours for short-crested wave ($k_x = k_y = \sqrt{2}/2\,\mathrm{m}^{-1}$) interaction with a porous cylinder ($G_0 = 1$) with a partial opening at $7/8\pi < \theta < 9/8\pi$ ($a = 2, 3, 4\,\mathrm{m}$).

DOI: 10.1002/fld

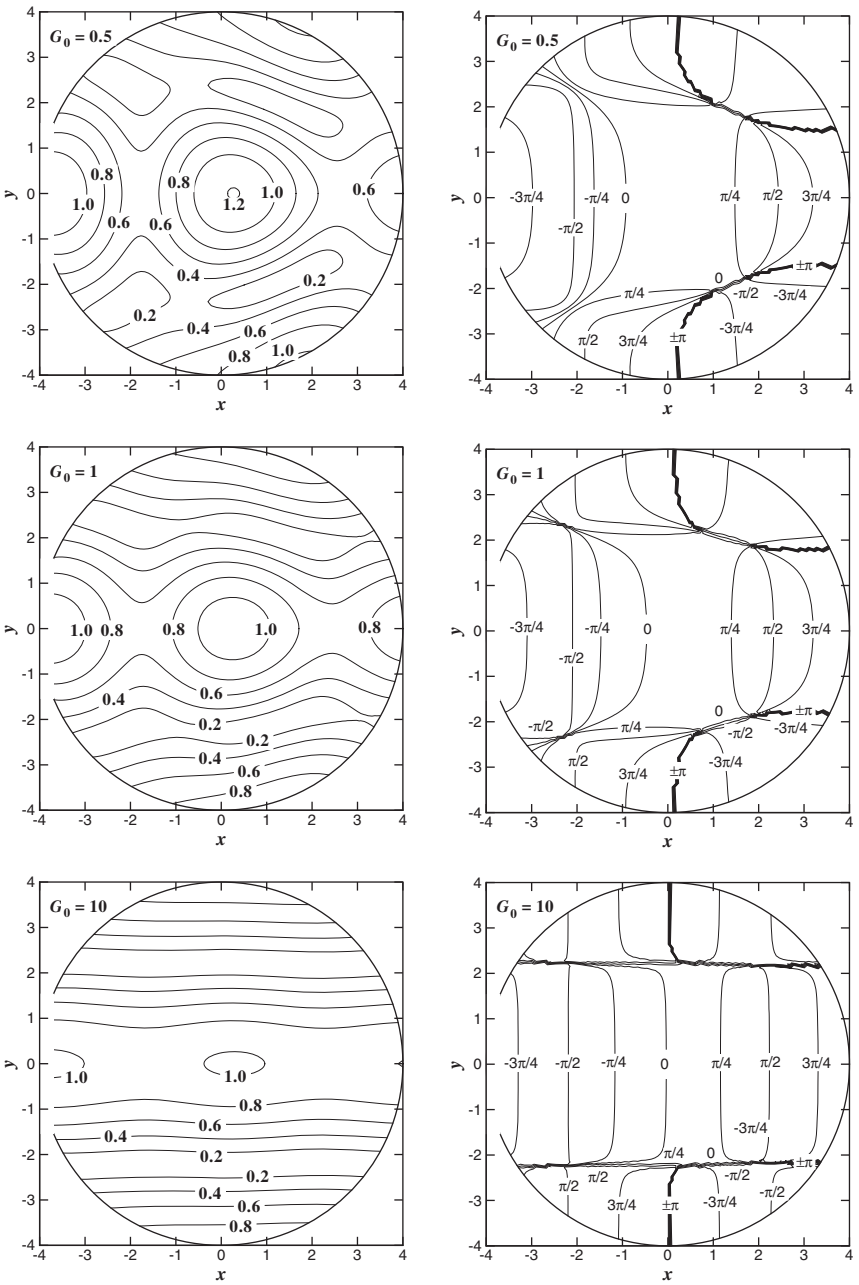

Figure 9. Equi-amplitude (left) and equi-phase (right) contours for short-crested wave ($k_x = k_y = \sqrt{2}/2\,\mathrm{m}^{-1}$) interaction with a porous cylinder ($G_0 = 0.5, 1, 10$) with a partial opening at $7/8\pi < \theta < 9/8\pi$ ($a = 4\,\mathrm{m}$).

DOI: 10.1002/fld

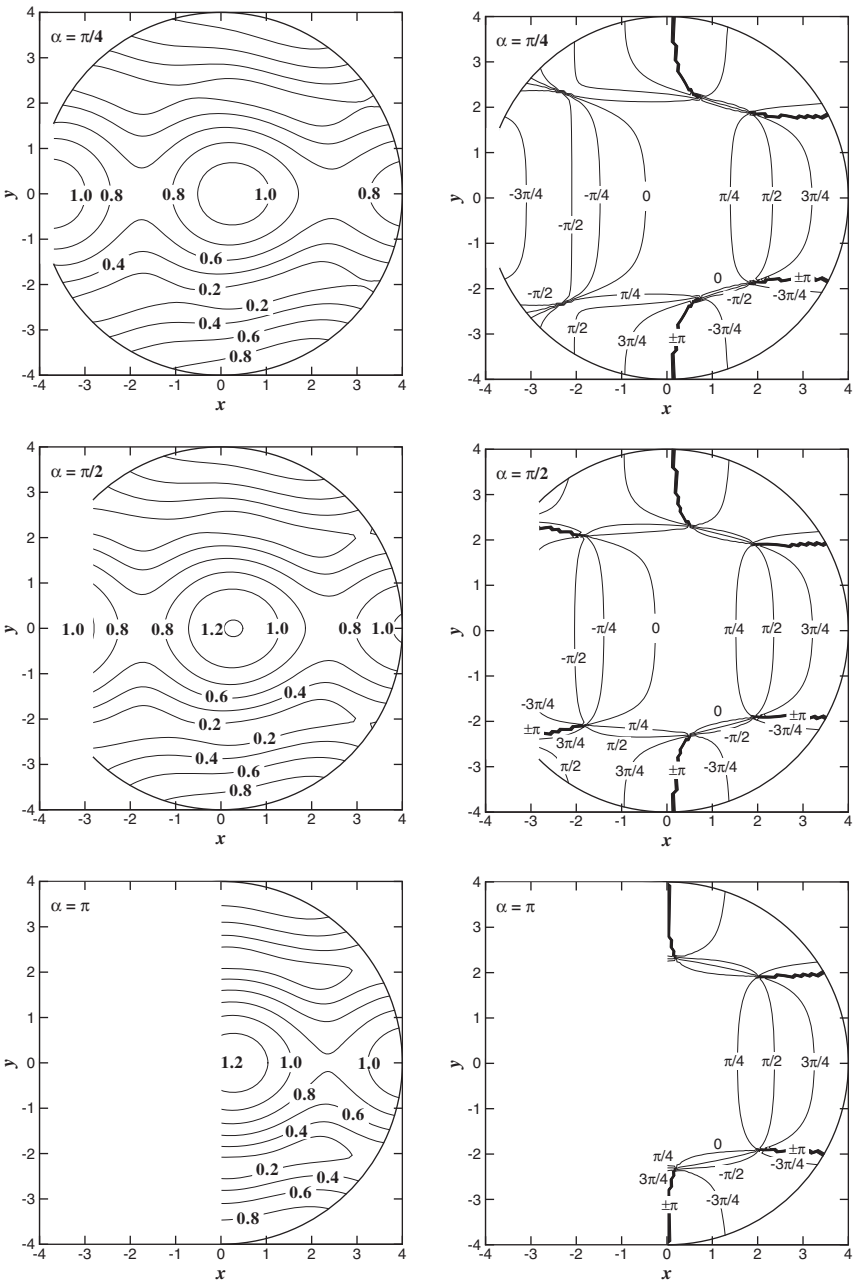

Figure 10. Equi-amplitude (left) and equi-phase (right) contours for short-crested wave ($k_x = k_y = \sqrt{2}/2\,\mathrm{m}^{-1}$) interaction with a porous cylinder ($G_0 = 1$) with a partial opening ($\alpha = \pi/4, \pi/2, \pi$) centred at $\beta = \pi$ ($a = 4\,\mathrm{m}$).

DOI: 10.1002/fld

The amplitudes in the inline directions are seen varying rapidly, while the transverse values change slowly for these three opening angles. It appears that the opening angle has rather limited effect on the equi-phase contour patterns.

6.1.4. Influence of opening location. The equi-amplitude (left) and equi-phase (right) contours for short-crested wave ($k_x = k_y = \sqrt{2}/2\,\mathrm{m}^{-1}$) interaction with a cylinder ($a = 4\,\mathrm{m}$ and $G_0 = 1$) with a partial opening ($\alpha = \pi/4$) at three different locations along the cylinder circumference direction, $\beta = \pi, \pi/2, 0$ respectively, are shown in Figure 11. It is seen that surface elevation in the interior region reduces as the opening location shift away from the incident wave direction, indicating more effective protection. Such an effect of increased protection by rearranging openings away from incident wave direction is expected to be more profound for a cylinder with low porosity.

6.2. Wave forces

6.2.1. Influence of G_0. The influence of ka on wave forces experienced by a cylinder with a partial opening at $\beta = \pi$ and opening angle $\alpha = \pi/4$ is also investigated for the same wave condition, $k_x = k_y = \sqrt{2}/2\,\mathrm{m}^{-1}$. Three cases of different porosities $G_0 = 0.5, 1, 10$, respectively, are calculated and the results are presented in Figure 12. For different G_0, a similar pattern of wave forces oscillating with ka is clearly observed. The porosity effect parameter is seen to have significant impact on the wave forces imposed on the cylinder, i.e. $|P_x|$ is markedly lower as G_0 increases indicating increased wave transmission. As ka increases, peak and trough attenuation is clearly evident for different G_0.

6.2.2. Influence of opening angle. The variations of the wave forces on a cylinder with a partial opening at $\beta = \pi$ by the incident short-crested wave of equal wave numbers ($k_x = k_y$) versus ka are shown in Figure 13 for $G_0 = 1$. The results plotted in Figure 13 are for three different values of opening angle $\alpha = \pi/4, \pi/2, \pi$, respectively. It can be seen that the wave forces fluctuate and peak attenuation is evident. Significant reduction in wave force fluctuation is clearly seen as the opening angle increases. For a cylinder of porosity $G_0 = 1$ with an opening of half circle ($\alpha = \pi$), Figure 13 shows that the wave forces rather smoothly decrease with ka after an initial rapid increase to a peak value.

6.2.3. Influence of opening location. Figure 14 shows wave forces on a porous cylinder ($G_0 = 1$) with a partial opening ($\alpha = \pi/4$) at five different locations $\beta = 0, \pi/4, \pi/2, 3\pi/4, \pi$, respectively. Again, the incident short-crested wave is of equal wave numbers, i.e. $k_x = k_y$. It can be seen clearly that the opening location is very sensitive at low ka to the inline forces but much less influence as $ka \geqslant 2$. As shown in Figure 14, trough attenuation is no longer seen as ka increases, while peak attenuation is found for all β values. The magnitude of the transverse wave forces shown in Figure 14 is rather small and becomes virtually zero for $\beta = 0$ and π since the corresponding configurations being symmetric to the x direction.

It is worthnoting that, the computational times (recorded on a 2 GHz Pentium IV PC and MATLAB 7.1) of the present SBFEM solutions are very small. For all cases presented in this paper, accurate results are obtained in less than 3 s, a clear demonstration that it significantly outperforms any current FEM or BEM for wave diffraction problems. Such computational efficiency and accuracy ensure great potential of direct application of the present model to many engineering problems especially in ocean engineering.

DOI: 10.1002/fld

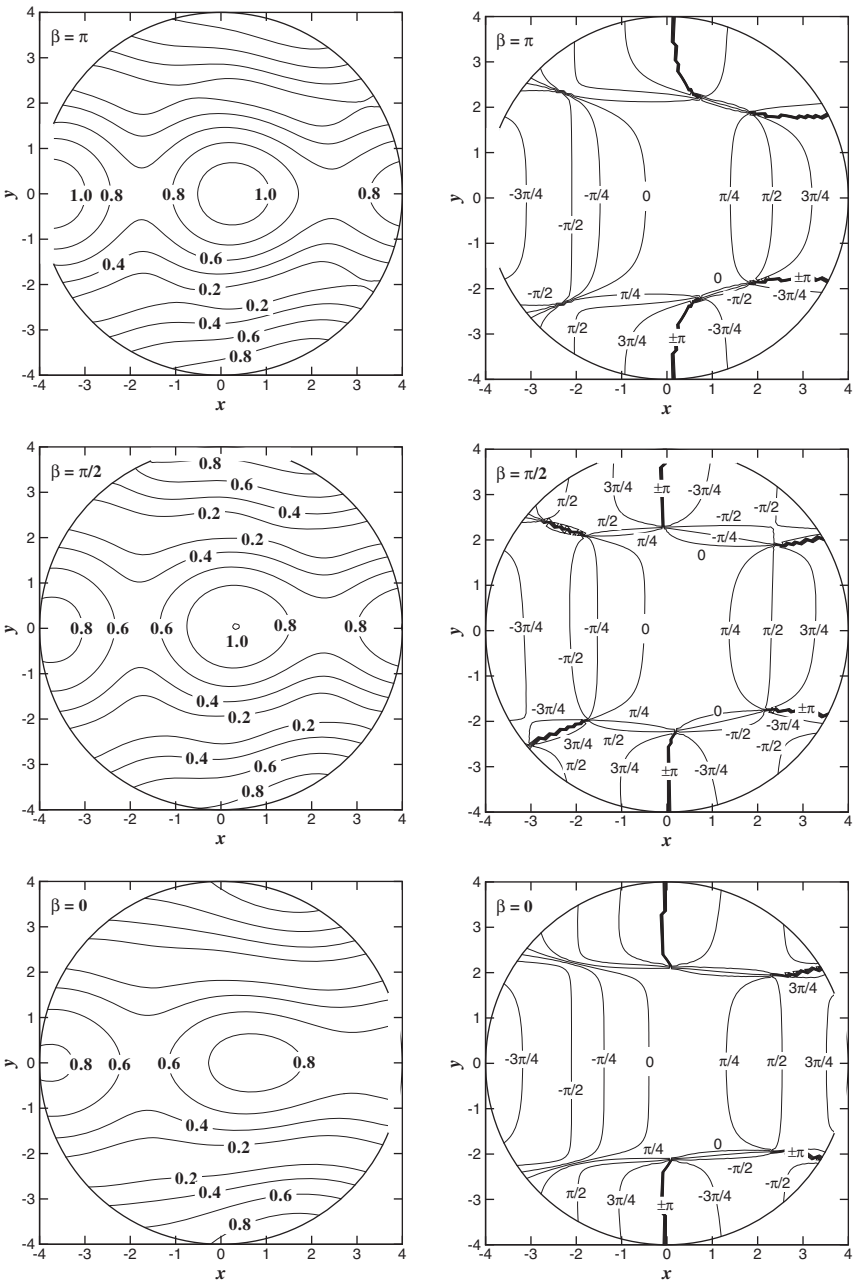

Figure 11. Equi-amplitude (left) and equi-phase (right) contours for short-crested wave ($k_x = k_y = \sqrt{2}/2\,\mathrm{m}^{-1}$) interaction with a porous cylinder ($G_0 = 1$) with a partial opening ($\alpha = \pi/4$) centred at $\beta = \pi, \pi/2, 0$ ($a = 4\,\mathrm{m}$).

DOI: 10.1002/fld

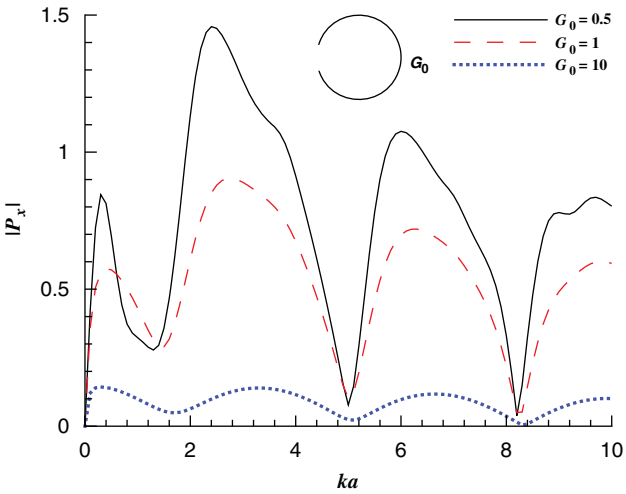

Figure 12. Wave forces versus ka for a cylinder with a partial opening at $\beta=\pi$ and opening angle $\alpha=\pi/4$ ($G_0=0.5, 1, 10$).

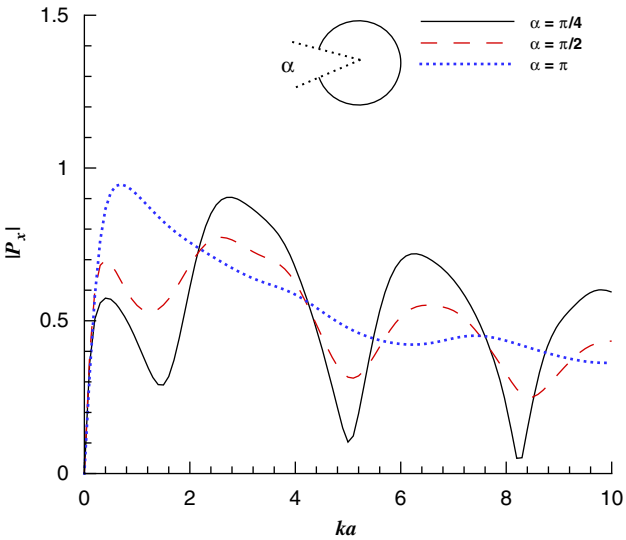

Figure 13. Wave force versus ka for a porous cylinder ($G_0=1$) with a partial opening at $\beta=\pi$ (opening angle $\alpha=\pi/4, \pi/2, \pi$).

DOI: 10.1002/fld

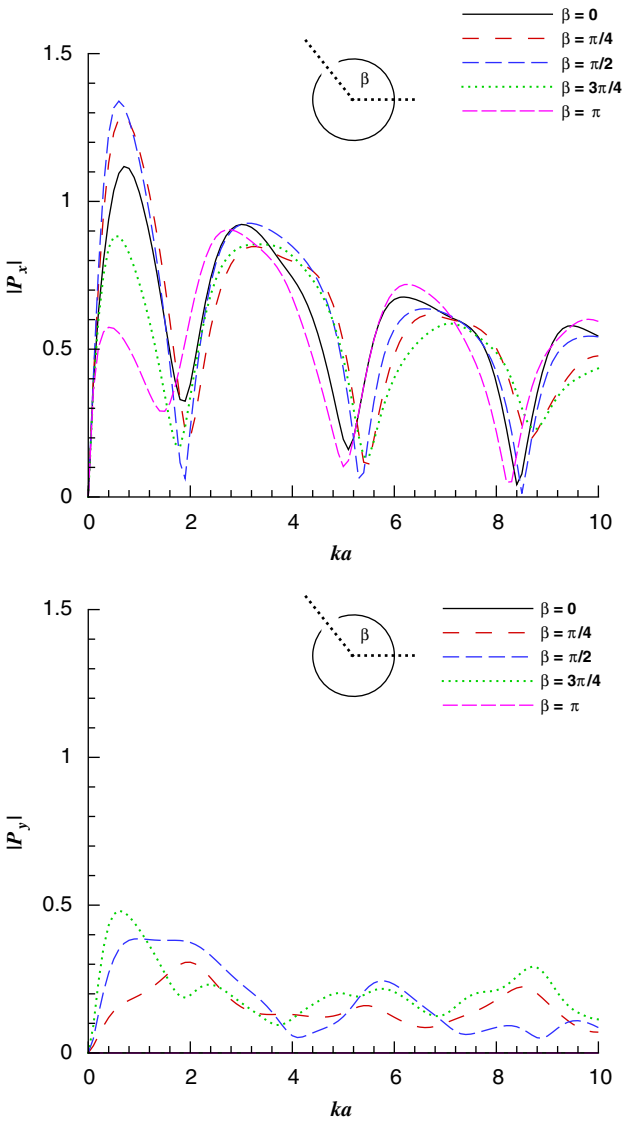

Figure 14. Wave force versus ka for a porous cylinder ($G_0=1$) with a partial opening ($\alpha=\pi/4$) at $\beta=0, \pi/4, \pi/2, 3\pi/4, \pi$.

7. CONCLUSIONS

The versatility of the newly developed semi-analytical SBFEM is demonstrated in this paper in considering the interaction of short-crested waves with a cylindrical structure with an partial solid wall or opening. By introducing a porous-effect parameter, the final SBFEE has been successfully transformed from non-homogeneous to homogeneous, and further solved in the frame work of the SBFEM. With no additional approximations being introduced, the SBFEM thus remains a

DOI: 10.1002/fld

semi-analytical fundamental-solution-less approach, but capable of dealing with much more complex structural configurations. Only the body boundary is discretized with surface finite elements. Excellent computational efficiency and accuracy of the SBFEM model have been demonstrated, as the governing equations are solved analytically in the radial direction. The influence of structural configuration including cylinder radius, porosity, opening angle and opening location is studied and the results in terms of the wave forces and surface elevations are presented. The results presented here should be found useful in the design of coastal and ocean structures.

ACKNOWLEDGEMENTS

The first author is grateful for the postdoctoral fellowship from Griffith University to support this research.

REFERENCES

1. Chwang AT, Chan AT. Interaction between porous media and wave motion. *Annual Review of Fluid Mechanics* 1998; **30**:53–84.
2. Chwang AT. A porous wavemaker theory. *Journal of Fluid Mechanics* 1983; **132**:395–406.
3. Chwang AT, Li W. A piston-type porous wavemaker theory. *Journal of Engineering Mathematics* 1983; **17**: 301–313.
4. Chwang AT, Dong ZN. Wave-trapping due to a porous plate. *Fifteenth ONR Symposium on Naval Hydrodynamics*. National Academy Press: Washington, DC, 1984; 407–417.
5. Faltas MS. On oblique waves forcing by a porous cylindrical wall. *International Journal of Mathematics and Mathematical Sciences* 1996; **19**(2):351–362.
6. Dalrymple RA, Losada MA, Martin PA. Reflection and transmission from porous structures under obliquewave attack. *Journal of Fluid Mechanics* 1991; **224**:625–644.
7. Yu X, Chwang AT. Wave motion through porous structures. *Journal of Engineering Mechanics* 1994; **120**(5): 989–1008.
8. Yu X, Chwang AT. Water waves above submerged porous plate. *Journal of Engineering Mechanics* 1994; **120**(6):1270–1282.
9. Wang K-H, Ren X. Water waves on a flexible and porous breakwater. *Journal of Engineering Mechanics* 1993; **119**:1025–1048.
10. Zhu S. Diffraction of short-crested waves around a circular cylinder. *Ocean Engineering* 1993; **20**(4):389–407.
11. Zhu S, Moule G. Numerical calculation of forces induced by short-crested waves on a vertical cylinder of arbitrary cross-section. *Ocean Engineering* 1994; **21**(7):645–662.
12. Song C, Wolf JP. The scaled boundary finite-element method—alias consistent infinitesimal finite-element cell method—for elastodynamics. *Computer Methods in Applied Mechanics and Engineering* 1997; **147**:329–355.
13. Wolf JP. *The Scaled Boundary Finite Element Method*. Wiley: Chichester, 2003.
14. Li B, Cheng L, Deeks AJ, Zhao M. A semi-analytical solution method for two-dimensional Helmholtz equation. *Applied Ocean Research* 2006; **28**:193–207.
15. Tao L, Song H, Chakrabarti S. Scaled boundary FEM solution of short-crested wave diffraction by a vertical cylinder. *Computer Methods in Applied Mechanics and Engineering* 2007; **197**:232–242.
16. Taylor GI. Fluid flow in regions bounded by porous surfaces. *Proceedings of the Royal Society of London, Series A* 1956; **234**:456–475.
17. Fuchs RA. On the theory of short-crested oscillatory waves. *Gravity Waves, National Bureau of Standards Circular No. 521*, Department of Commerce, U.S.A., 1952; 187–200.
18. Tao L, Song H, Chakrabarti S. Wave interaction with a perforated circular breakwater of non-uniform porosity. *Journal of Engineering Mathematics* 2008; DOI: 10.1007/s10665-009-9287-x.